

Detection of a transiting Hot Jupiter around WASP-44

Adriana Barbieri

Alessandro Bianchetti

January 17, 2022

Abstract

In the following report we work on WASP-44 b, an exoplanet orbiting around its G-type parent star, located in the constellation of Cetus. We first examine its atmospheric parameters and derive its mass and radius (Morton 2015). Then, we correct for limb darkening effect through different methods (Claret et al. 2011, Claret 2017, Claret 2018). We also take some images obtained with Copernico telescope at the Asiago Observatory into consideration and, after proper correction, we use them to extract the light curve of the alleged planet.

1 Introduction

Confirmed exoplanets are growing in number year by year, and transit method is nowadays a widespread and hugely successfull detection method. Most planets indeed are by now discovered by tracing the lightcurve and searching for any sign of a weakening in the flux.

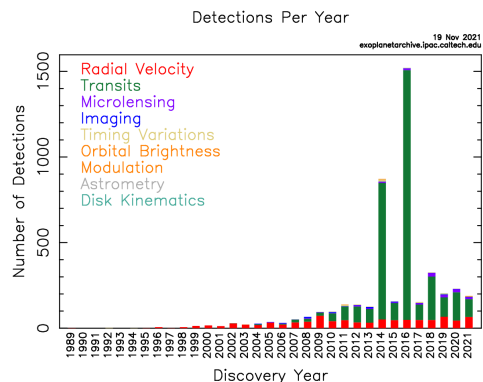


Figure 1: Confirmed exoplanets distribution per year of detection via different methods. Credits to <https://exoplanetarchive.ipac.caltech.edu/>

In this report we focus on WASP-44 b, a

Jupiter-size planet orbiting around a G-type star, located in the constellation of Cetus. Among the numerous available reports on the planet, we decided to make a conservative choice and avoid any result which is not inferred via spectroscopy. This leads us to rule out several papers regarding our target of interest and exclusively work with the discovery paper (Anderson et al. 2011). In this paper, estimates of the atmospheric parameters of WASP-44 are provided via an analysis of the width of the spectral lines.

2 The transit method

The transit method is a photometric indirect method of detection of exoplanets, which consists in the observation of a drop in the flux of a star due to the transit of a planet across the stellar disk.

The subsequent variation of the measured stellar luminosity is proportional to the ratio of the projected areas of the planet and the star, or equivalently, the dimming of the flux

is proportional to the ratio of the square of the respective radii; therefore, known the radius of the star from its spectrum, the radius of the planet can be easily obtained from the measured depth of the flux.

Moreover, if combined with radial velocities measurements, this method allows to compute also the average density of the exoplanet.

It is important however to notice that limb darkening, stellar activity and atmospheric effects may pollute the observational transit curve and must be all taken into account.

The modelled transit light curve is distinguished by a characteristic trapezoidal shape, whose main geometrical parameters are the impact parameter, the ingress/egress and transit duration, and the transit depth.

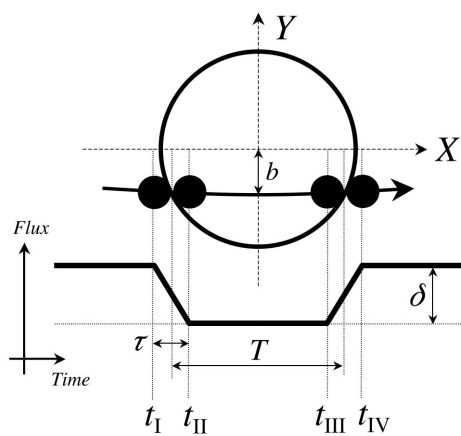


Figure 2: Simplified transit light curve. Credits to Winn [2010]

The geometry of the system places a strong constraint on the inclination of the orbital plane of the planet with respect to the line of sight: the transit can be observed exclusively for almost edge-on orbits, meaning orbital planes that are as parallel as possible to the line of sight. This condition yields a low probability of detection, which in turn requires a huge number of target stars to carry on successful observations.

Furthermore, at least two transits are required to determine the orbital period of the extrasolar planet candidate, and since the duration of the transit is very short compared to the orbital period, continuous and prolonged observations are required in order to detect it.

It is of capital importance to be aware of the selection biases that are intrinsic to this method (and to the current available technology): indeed it yields the largest detection probability for large massive planets orbiting very close to small and quiet stars, thus selecting Hot Jupiters around late type stars as ideal targets.

3 Preliminary steps

3.1 Inferring mass and radius

The H_{α} line was used to determine the effective temperature (T_{eff}), while the $NaI D$ and $MgI b$ lines were used as surface gravity ($\log g^*$) diagnostics (Anderson et al. 2011). The elemental abundances, including $[Fe/H]$ were determined from equivalent width measurements of several clean and unblended lines. This led to proper estimation of the atmospheric parameter triplet T_{eff} , $\log g^*$ and $[Fe/H]$. Quoted errors include statistical uncertainties only. In the same conservative spirit we previously showed, we add in quadrature a further term to the errors of all three parameters (Sousa et al. 2011). We are in fact more interested in an accurate result rather than in a precise one. This leads to the following results

T_{eff} (K)	$\log g^*$	$[Fe/H]$
5400 ± 162	4.5 ± 0.2	0.06 ± 0.11

We then ran *isochrones* (Morton 2015), with Bayesian approach, with posterior sampling performed by *MultiNest* and including Gaia parallax $p = 2.764 \pm 0.020 \mu as$. These are the results of the analysis:

Parameter	Value
$M(M_\odot)$	0.95 ± 0.05
$R(R_\odot)$	0.93 ± 0.01
$\rho(\rho_\odot)$	1.19 ± 0.09
$age(Gyr)$	$4.8^{+3.5}_{-2.9}$

Huge errors on the age estimate are pretty common for this analysis, since stars with this mass evolve very slowly along the Main Sequence.

3.2 Limb darkening correction

Limb darkening is an important effect that cannot be neglected when observing a star. In short, the edges of the luminosity profile of a star always look darker than the core: this occurs because there is a physical, constant distance L at which the optical depth is equal to unity, further than which the observations are not possible since photons are completely absorbed and do not reach the observer. This characteristic size, however, can extend deep inside the hot layers of the star if we look straight to the center, being L radial, while it can stop at the colder, outer layers if we look at the edges of the star, since L and our line of sight (LoS) are not radial anymore.

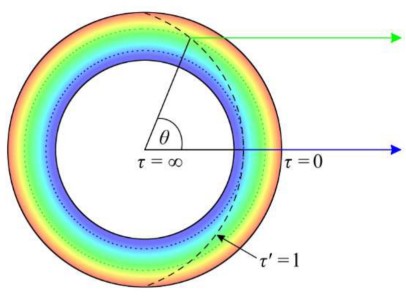


Figure 3: Limb darkening effect scheme. Credits to <https://ediss.sub.uni-hamburg.de>

Correcting for this effect may be challenging. Indeed we can measure it directly only for the Sun, while we need to model it somehow for any other star, thus figuring out a

proper law for the intensity decrease $I(\mu)$, where $\mu = \sqrt{1 - r^2}$. Many choices are plausible at this point: a uniform behaviour, a linear, a quadratic, a square-root or a logarithmic law are all valid guesses. Parametrizing such laws introduces the so-called *LD-coefficients*, which will depend on the stellar parameters. Knowing the latter relationship (for instance calibrating it based on a large sample of stars) allows to obtain the coefficients directly from the atmospheric parameters. The alternative way is fitting the light curve leaving the coefficients as free parameters.

The choice of the functional dependence on μ is a delicate one. Multiple approaches can be followed, basing on different papers. This analysis is addressed in A.

4 TASTE data analysis

Before actually analysing data from TASTE, we need to properly correct them. Then, we're going to have a look at and correctly format them, preparing the configurations file for the PyORBIT run.

4.1 Bias and flat field correction

CCD s(Charged Coupled Devices) are the privileged detectors for photon counting, due to their high quantum efficiency. The images produced are *raw* and must be properly *pre-reduced* before being analysed. Pre-reduction goes through different steps:

- **bias** is the individual pixel-to-pixel offset level, and it is a zero-exposure instrumental factor, thus it is always an added contribution to any signal. Therefore it must be removed in order to isolate the photons of astrophysical origin. The root mean square of the bias corresponds to the so-called *readout noise*. We perform an average across all the pixels to get an estimate

of the bias;

- a **flat field** is a calibration image obtained by illuminating homogeneously the pupil of the telescope, using twilight sky or appropriate, back-lighted screens. This correction factor is to be applied on each pixel and then also normalised, after the overall bias correction;
- **differential photometry** is a great way to keep track of any noise variation. The idea is to take a reference star close enough to the target: any environmental or instrumental variation will affect both sources. Working with flux ratios will make only astrophysical variations evident!

For pre-reductions steps, we use the code *huggy*. We first perform bias correction, than the flat field correction. The corrected images are ready for aperture synthesis.

4.1.1 Bias correction

We run *huggy-bias.e* inputting the raw images.

`huggy-bias.e A*.fits`

Many bias images are produced, displaying the zero offset of the pixel board. *Master bias* is the average of all these files. Plotting the intensities of the offset level of the pixels yields a concrete view of the correction. Note that the master bias frame distribution is peaked and much closer to a unique constant value, as all pixels behaved in the same way, like in an ideal situation. We can see this even numerically, by looking at the dispersions of the above distributions: $\sigma_{rb} = 3.82$ and $\sigma_{mb} = 0.89$.

4.1.2 Flat field correction

We now run *huggy-flat.e* inputting a normalization fraction, meaning the fraction of pixels

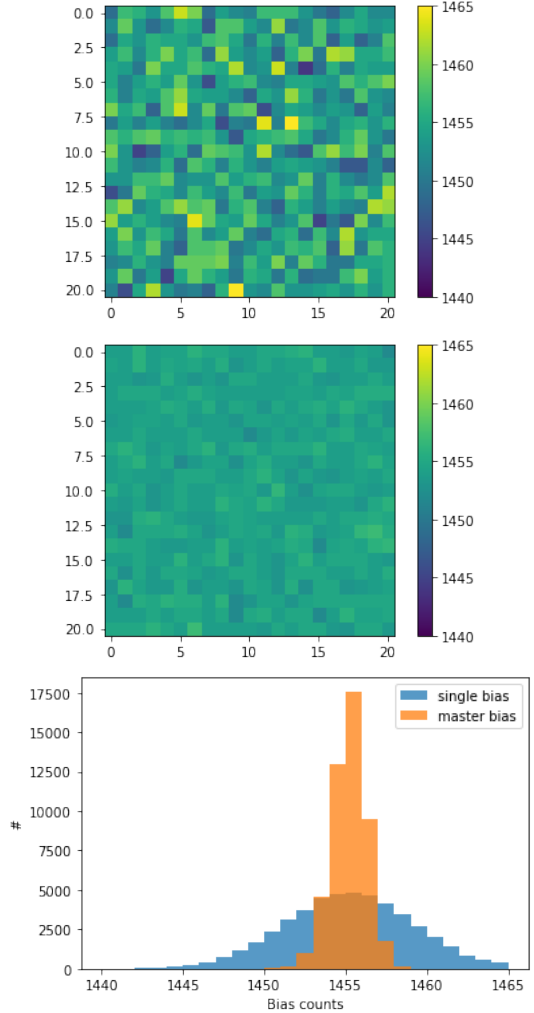


Figure 4: Comparison between random bias frame and master bias

we want to account for, ruling out the sides which are often polluted by overscan columns. These are visible in the form of dark stripes on the sides of any flat field take. Then we have to input the overscan values, usually set to 0. Subsequently, we need to provide the master bias file, which will be subtracted from the data. Finally, we input all the available flat fields.

```
huggy-flat.e 0.9 0 0 mb.fits A*.fits
```

This will produce an output file showing the average response of pixels to an external light source. Minor differences in such response are important and must be accounted for.

4.2 Final correction

The final step is applying the correction files obtained in the previous parts.

```
huggy-correct.e mb.fits mfn.fits A*.fits
```

The final correction code requires the master bias and the normalised master flat, and of course all the target images, that are all going to be corrected.

4.3 Extracting the light curve

We are approaching the very heart of this analysis, preparing for aperture synthesis. We now need to display the science images, make sure to identify the correct target and select a proper background analysis around it. To do that, we have to properly circle the source and create a slightly larger circle around it (we used the *ds9* tools). The same procedure must be repeated (with the same inner and outer radii) on a properly selected reference star, close to and roughly as bright as the target. We hereby report the coordinates of the target and of the chosen reference star, in pixel units.

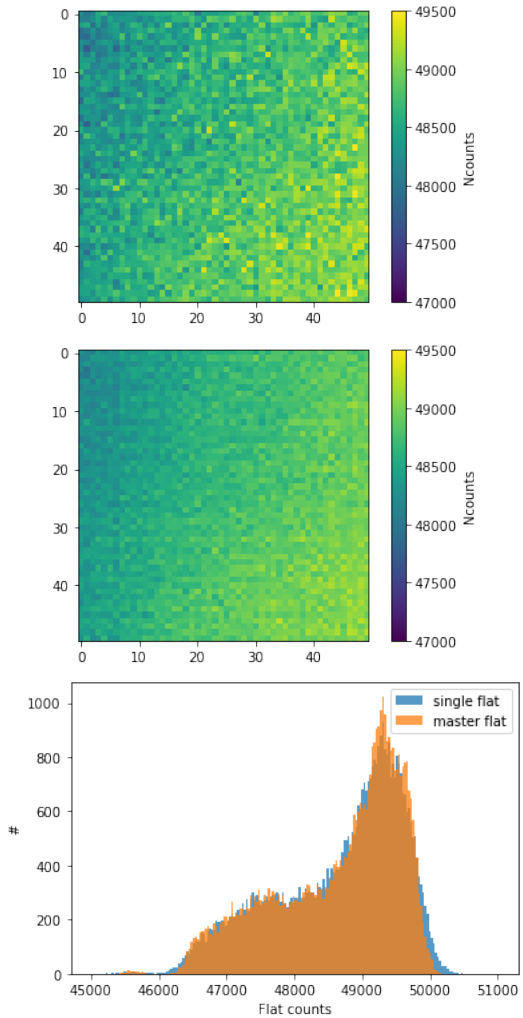


Figure 5: Comparison between random flat field and master flat

	x_c	y_c
Target	170	37
Reference	288	57

$R_{in} = 11, R_{out} = 20$

Now we need to call *huggy-psf.e* and input the coordinates of the center of the target, the inner and outer radii, and a random corrected image.

```
huggy-psf.e x0 y0 Rin Rout A*.fits
```

This yields information about the Point Spread Function, meaning how the flux is distributed as a function of the distance from the core of the source. The output displays the radii at which we find 90, 95 and 99% of the total flux. The three apertures in pixel units are $a_0 = 4.71$, $a_1 = 5.97$ and $a_2 = 8.76$, respectively for 90, 95 and 99%. We take note of this output.

Photometry analysis is carried out by *sentinel.e*, which needs the coordinates of the target and of the reference stars, followed by the radii of two selected apertures from the previous output. Also, we need again inner and outer radii of the selected region for the analysis, as well as the full-corrected images of the target.

```
sentinel.e x0 y0 xr yr a1 a2 Rin Rout c
A*.corr.fits
```

where $c = \{1, 2\}$ selects the centroiding method (gaussian/moment). For a star fainter than average like ours ($J \approx 11$) the recommended choices for the apertures are 90 and 95%, in order to make sure not to run into saturation. However, all three possibilities were tested.

The *sentinel* output is the starting point for TASTE analysis. This file contains the main information about the target and the sky, keeping track of the respective photometries. In fact, we check the evolution of the sky

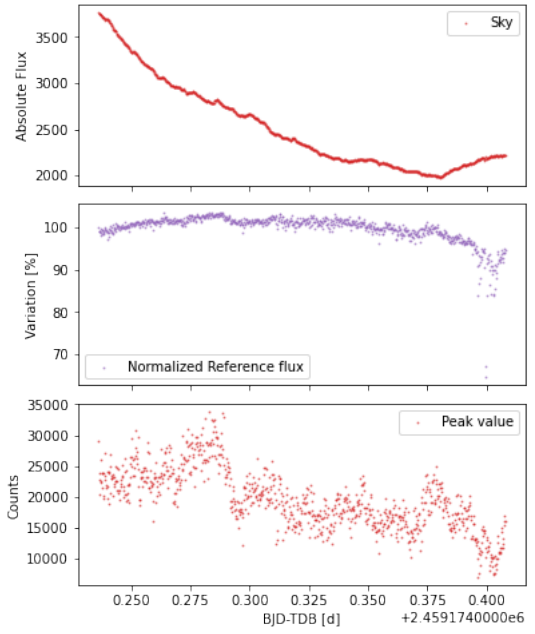


Figure 6: Upper panel: sky background flux, every point is the median of the annulus formed by R_{in} and R_{out} . Middle panel: reference star flux, normalised to the first measurement. Bottom panel: peak points of the flux inside the defined aperture.

background throughout the observation session, and also to the behaviour of the reference star (6). The sky flux has been constantly decreasing in time, so we expect less and less disturbance as the observation proceeds. The reference star, on the other hand seems to be pretty stable in terms of flux. We also want to make sure that reference star are correctly comoving: to do that, we plot the variation in position at every time step and make sure we have similar motion (7). Plotting FWHM reveals an increasing trend, at odds with the sky pattern. Next, we compare the flux plot of all three different aperture we have chosen (8). The second case (99%) seems to be slightly less noisy: that's our first clue that this aperture might be the best suited choice for the aperture analysis. As a further goodness check, one may take a look at the peak value trend of the

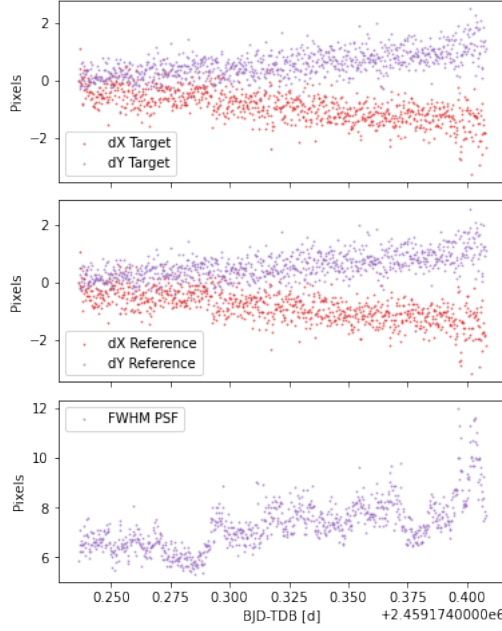


Figure 7: Upper and middle panel: target and reference star show the same coordinate variation in the CCD. Bottom panel: full width half maximum of the peak flux.

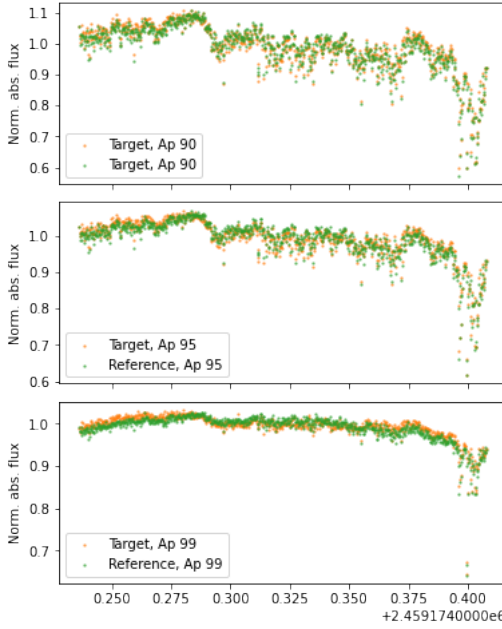


Figure 8: From top to bottom: 90, 95 and 99% apertures, showing both the target and reference star. Dispersion is reduced as the aperture grows.

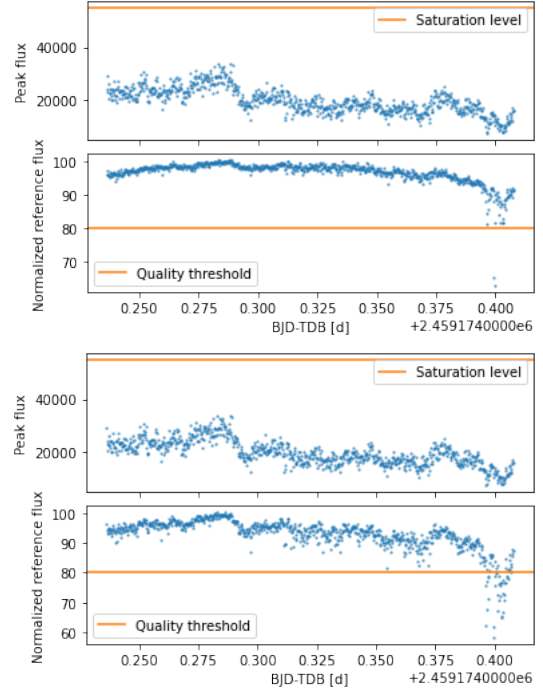


Figure 9: Upper panel: narrow apertures, bottom panel: wider apertures. In both cases the peak value is well below the saturation limit, and we also see that the reference data are above the required threshold. A few points at late times are below the quality factor for the 90-95% case, thus supporting the choice of the widest aperture at 99%.

target source and compare it to the saturation level. We also plot the reference star flux to see whether they are above the quality threshold.

We can finally visualise the transit in all three cases. To do that, we plot the ratio between target and reference star: *differential photometry* helps us get rid of systematic errors affecting both sources. We still see that the wider aperture seems to have less dispersion than the other case, and we keep that in mind.

In order to evaluate the depth of the transit, we need to identify the "height" of the continuous level: to do that, we need to exclude the transit datapoints and try out a polynomial

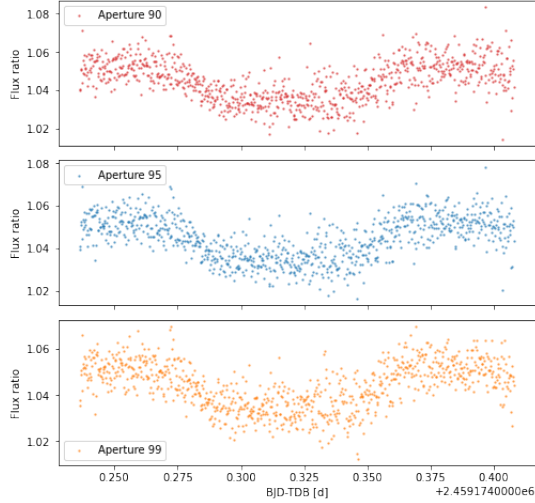


Figure 10: Transit image for growing aperture, top to bottom. Note that the above case (90%) shows the most outliers.

fit, hoping to find a perfectly horizontal line. That will be our reference trend for the stellar flux. To perform the fit, we ruled out all the points during the transit by roughly selecting an ingress and egress time. A quadratic law ($p_0x^2 + p_1x + p_2$) was chosen to set things up in the most general case. A least square fitting via numpy function `np.polyfit` yields Fig.12.

# ap	$p_0(\cdot 10^{-10})$	$p_1(\cdot 10^{-7})$	$p_2(\cdot 10^3)$
90	-1.19	1.43	0.72
95	-7.98	1.43	4.82
99	-8.98	1.42	5.43

We immediately notice that both p_0 and p_1 are well compatible with zero, meaning that only a constant term survives: that represents the level of the continuous.

After the fit, we also considered discarding outliers: however, a quick analysis reveal that all point are well within 5σ . Actually, except for the 90% aperture, even a more strict 3σ criterion would not rule out any data point.

We display the standard deviation of the points of the continuous with respect to the

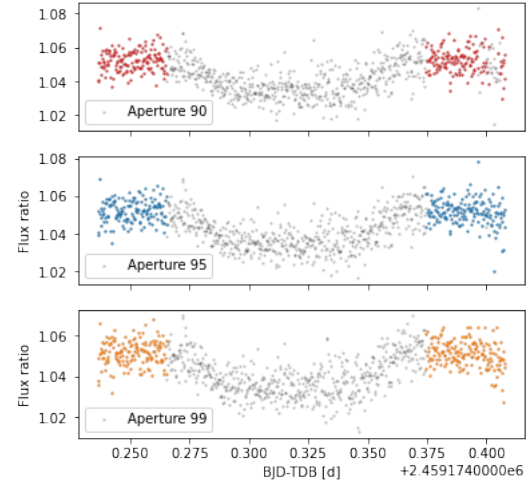


Figure 11: Time boundaries for the transit are roughly ballparked to prepare a proper, flat dataset to fit with a straight line.

linear fit. These quantify scattering and indicate that the 99% aperture is indeed the best photometric choice, having the smallest standard deviation.

σ_{90}	0.0063
σ_{95}	0.0061
σ_{99}	0.0059

5 TESS data analysis

5.1 Light curve extraction via aperture photometry

WASP-44 was observed by TESS (Transiting Exoplanet Survey Satellite) in 120s-cadence mode during observations of sector 3, between 2018 September 20 and October 17.

The photometric observations for WASP-44 were reduced by the Science Processing Operations Center (SPOC) pipeline (Jenkins et al. 2016).

From ExoFOP-TESS¹ we retrieved the TIC

¹Exoplanet Follow-up Observing Program for TESS website, to be found at <https://exofop.ipac.caltech.edu/tess/>

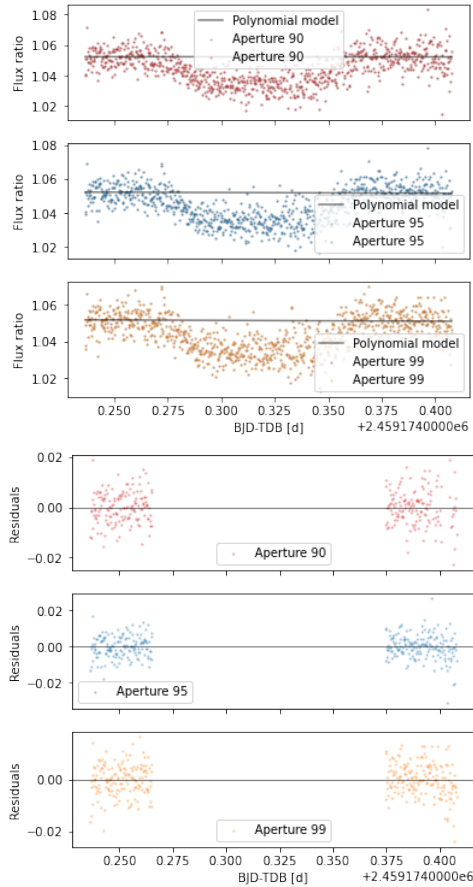


Figure 12: Horizontal fit and residuals for the three cases.

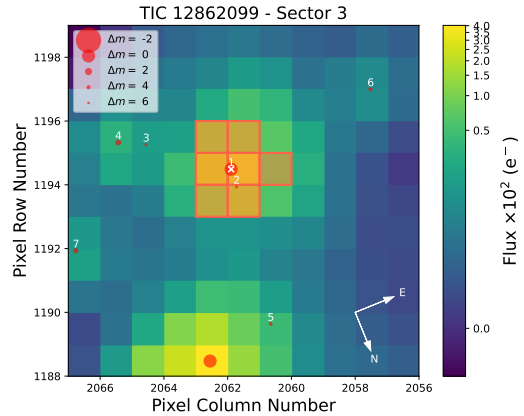


Figure 13: TPF plot.

(TESS Input Catalog) identification number for our target star (12862099). We were able then to download the 2-min cadence target pixel file (TPF), the SAP (Simple Aperture Photometry) and PDGSAP (Pre-search Data Conditioning Simple Aperture Photometry) flux files from the Mikulski Archive for Space Telescopes (MAST)², after previous selection of the data exclusive to the TESS mission.

We performed a preliminary contamination check with *tpfplotter*³, aiming to establish whether our default photometric aperture includes any contaminant star that may cause a dilution of the transit.

By running

```
python tpfplotter.py 12862099 --maglim 6
--SAVEGAIA
```

we obtained 13, which shows how only one star is present within the aperture, but since it is over 4 magnitudes fainter than the target in the G band, it does not constitute a contaminant and can therefore be ignored.

In order to obtain an independent confirma-

²<https://mast.stsci.edu/portal/Mashup/Clients/Mast/Portal.html>

³<https://github.com/jlillo/tpfplotter.git>

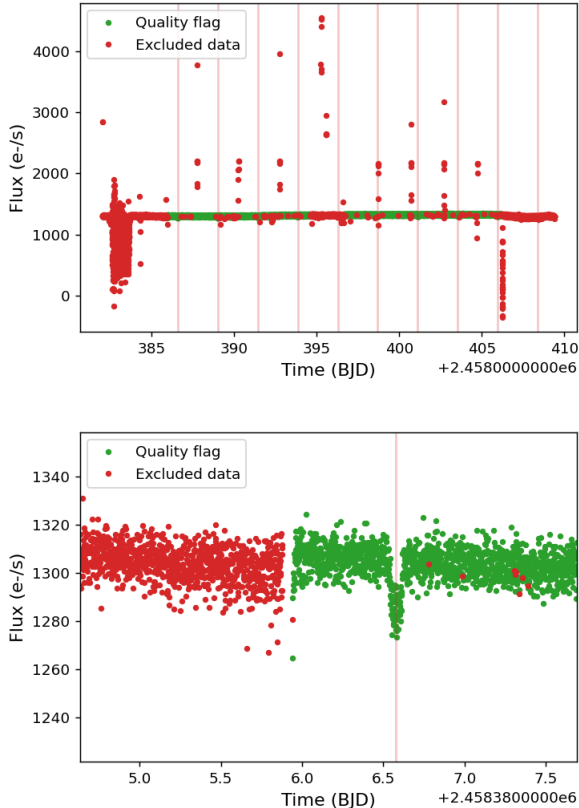


Figure 14: Flux derived from the calibrated pixels (up) and detail of the first cadence (bottom).

tion of the signals detected in the TESS light curve, we performed an iterative transit search on the detrended light curve using the Transit Least Squares method. Due to the fact that we’re combining information coming from many transits, the results are probably going to be more precise than TASTE.

We proceeded to perform aperture and time series photometry on the TPF in order to select only the pixels belonging to the optimal aperture; from the obtained calibrated pixels, we derived the transit and the background flux light curves. Afterwards we removed from the time series dataset of the optimal aperture all the TESS cadences flagged as anomalous or encoded as NaN, as can be seen in 14 .

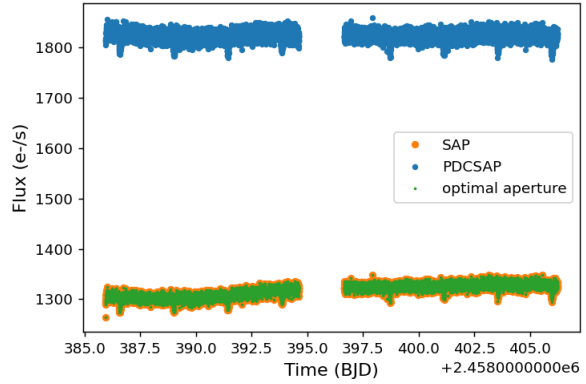


Figure 15: Optimal aperture, SAP and PDCSAP lightcurves.

Subsequently we repeated the quality selection analysis on the lightcurve files (provided by the TESS team and obtained from the MAST portal as previously addressed), and plotted both the optimal aperture, the SAP and the PDCSAP fluxes thus obtained as a function of time (15). The observed overlapping between the optimal aperture and the SAP lightcurve is evidence for the goodness of the analysis. For our photometric analysis, however, we will make use of the PDCSAP light curve, being it usually cleaner than the SAP flux and also corrected for systematic trends.

5.2 Detrending methods

It is of capital importance to flatten and detrend the light curve, meaning to correct for stellar activity, flares, gaps in the data and interrupted transits by removal of the curve modulation due to the stellar and instrumental systematics. Via the *WOTAN* package⁴ (Hippke et al. 2019a) we applied to the PDCSAP light curve a biweight filter with a time window of 1 d and a hspline filter with a time window of 2 d (16); afterwards we normalized and folded the lightcurves, with the aim of

⁴<https://github.com/hippke/wotan>

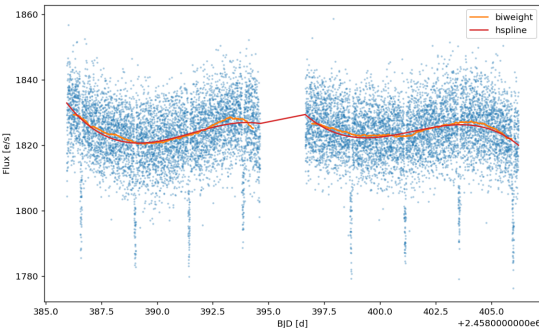


Figure 16: Outliers exclusion and time windowing

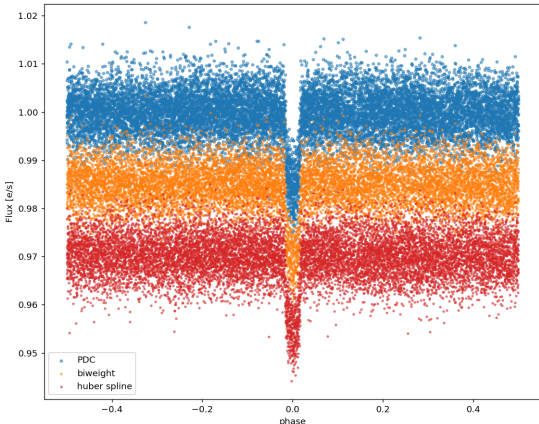


Figure 17: Flattened and folded data

studying the transits in phase (17).

We obtained for the PDCSAP, biweight and hspline fluxes' standard deviations the values of 0.00440736, 0.00406469 and 0.00407942 respectively. Therefore, having the smallest σ , we considered the flattened biweight lightcurve as the most accurate one.

5.3 Identification of periodic signals

We proceeded to perform an iterative transit search on the detrended light curve in order to independently confirm the detection of the periodic signals in the TESS light curve. We

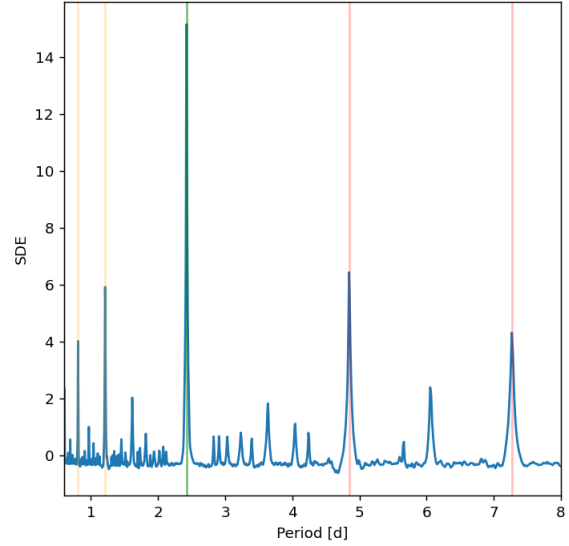


Figure 18: TLS periodogram

used the Transit Least Squares (TLS)⁵ algorithm (Hippke et al. 2019b), which offers one of the best method to detect planetary transits from time-series photometry. Indeed it searches for transit-like features with stellar limb-darkening, includes the effects of planetary ingress and egress, analyses the entire data of the phase-folded light curve and yields a $\approx 10\%$ higher detection efficiency (SDE) compared to the Box-fitting Least Square (BLS) method, therefore being more accurate but more time-consuming.

We obtained the periodogram (18) and folded lightcurve (19) with a SDE of 15.15413, a period $P = 2.42547d$, a central transit time $T_c = 2458386.57308BJD$ and a best transit duration of $0.07180d$ (roughly $1h43min$).

At last, we chose to select only the data points that are at a distance which is within twice the value of the transit duration from the center of the transit, we saved the output

⁵<https://github.com/hippke/tls>

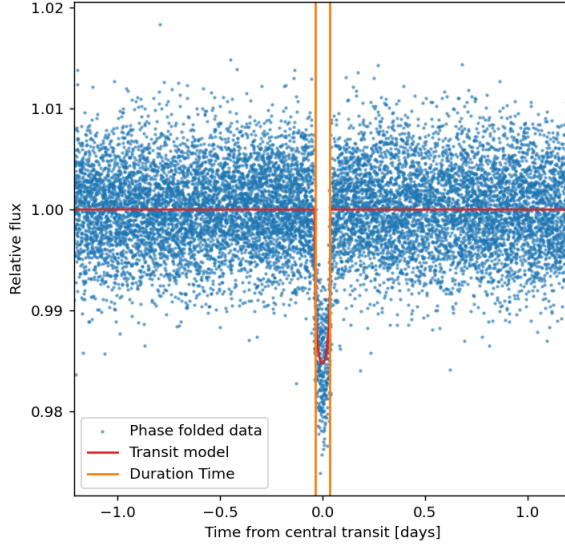


Figure 19: Detrended transits

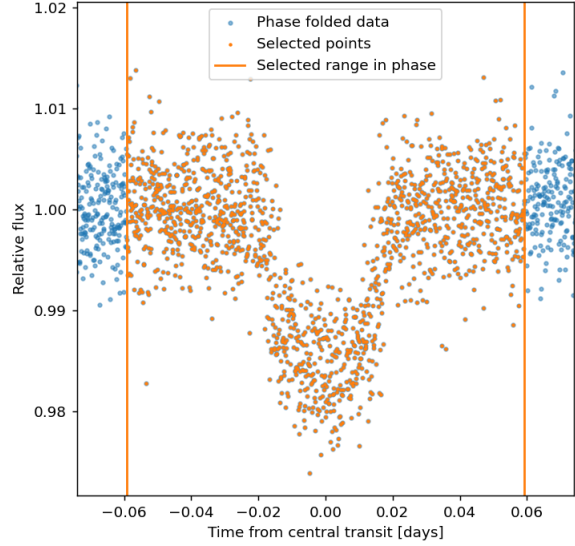


Figure 20: Final selection

in a data file that will be the basis for the subsequent analysis and we plotted the resulting transit light curve.

6 Light curve fit

Once obtained the datasets and prepared the .yaml configuration files both for TASTE and TESS, we proceeded to fit the transit light curves with a planetary model.

To this aim we performed the analysis using *PyORBIT*⁶ (Malavolta et al. 2016, Malavolta et al. 2018), a framework for the characterization of planetary systems that is able to analyse photometry, RVs and ancillary data and model stellar activity and transit time variations.

All the planetary transits were modelled using the Python package *BATMAN* (Kreidberg 2015); we used also the differential evolution tool *PyDE*⁷ in combination with the affine-invariant Markov chain Monte Carlo (MCMC) sampler *EMCEE* (Foreman-Mackey 2013) to perform global optimization of the input parameters and an autocorrelation analysis of the

⁶<https://github.com/LucaMalavolta/PyORBIT>

⁷<https://github.com/hpparvi/PyDE>

chains.

In the chosen models the orbits were assumed to be tidally circularized, and a flag was activated in order to add a jitter parameter in quadrature to the flux error to compensate for their under-estimation.

For the Bayesian analysis of the lightcurve, we assumed a circular orbit, quadratic law for the limb darkening coefficients, uniform priors for the period, the central time of transit, the impact parameter, scaled planetary radius, and gaussian priors for the stellar parameters.

For the Bayesian analysis of the TESS lightcurve, we chose a second order polynomial trend as a model for out of transit flattening, gaussian priors for the period, the limb darkening coefficients, the stellar parameter and uniform priors for all the other parameters.

Since the resulting chains were more than 50 times longer than the autocorrelation function, we are assured that the estimate can be trusted.

The physical parameters obtained from the posterior samples are collected in tables 1 and 2 in the following sections.

The corner plots of the posterior samples showing the correlation between the parameters are reported in Fig. 37, 38 and 22 .

Along the diagonal there are histograms of the estimated 1D posterior probability distribution for each parameter.

The histograms show that the recovered parameters are both accurate (close to injected value) and precise (narrow posterior distribution).

The off-diagonal plots are the 2D histograms of the estimated joint posterior probability distribution of each pair of parameters, which show the correlation between pairs of parameters.

The normalized stellar fluxes, fitted with the model of the exoplanetary transit, along with the residuals are reported in Fig. 21 and 23 .

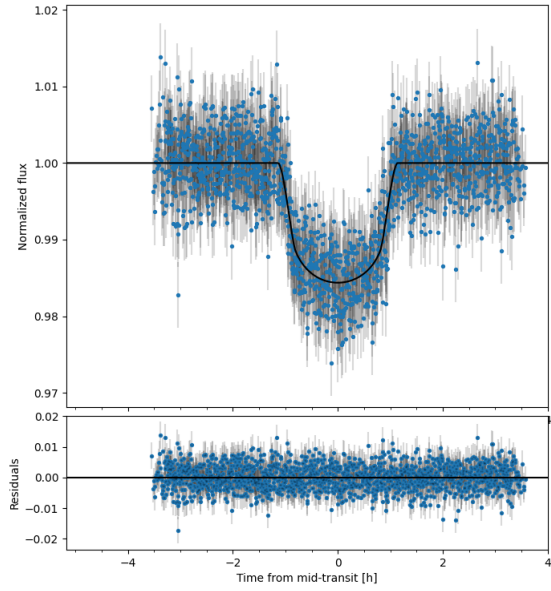


Figure 21: TESS lightcurve

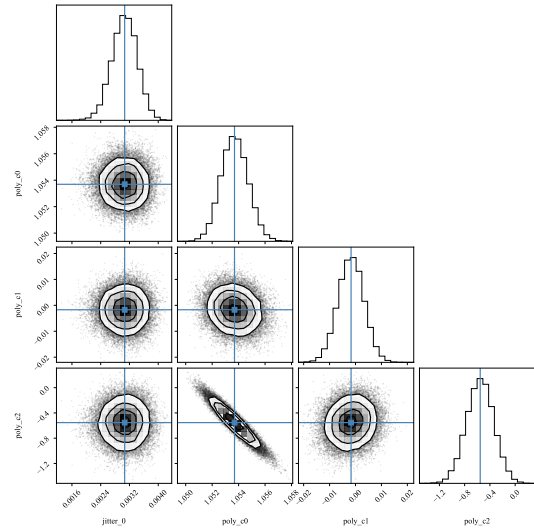


Figure 22: TASTE polynomial trend corner plot

Parameter	Value	σ_-	σ_+
$P(d_{BJD})$	2.423846	0.000168	0.000167
$T_c(d_{BJD})$	2458386.578204	0.000720	0.000721
b	0.526068	0.052957	0.047805
R_P/R_\star	0.116950	0.002680	0.002595
$\rho(\rho_\odot)$	1.209717	0.088844	0.090123
$c1_{ld}$	0.509840	0.282570	0.257019
$c2_{ld}$	0.167904	0.392996	0.396461
jitter	0.000241	0.000141	0.000219

Table 1: Physical parameters obtained from TESS analysis

Parameter	Value	σ_-	σ_+
$P(d_{BJD})$	2.468733	0.158915	0.131093
$T_c(d_{BJD})$	2459174.317823	0.000566	0.000554
b	0.585133	0.051438	0.042263
R_P/R_\star	0.129397	0.003821	0.003747
$\rho(\rho_\odot)$	1.156424	0.088183	0.090487
$c1_{ld}$	0.345531	0.090242	0.091553
$c2_{ld}$	0.230632	0.098916	0.099288
jitter	0.003067	0.000359	0.000341
p_0	1.053690	0.001014	0.001026
p_1	0.001706	0.004975	0.004923
p_2	0.553433	0.218298	0.211560

Table 2: Physical parameters obtained from TASTE analysis

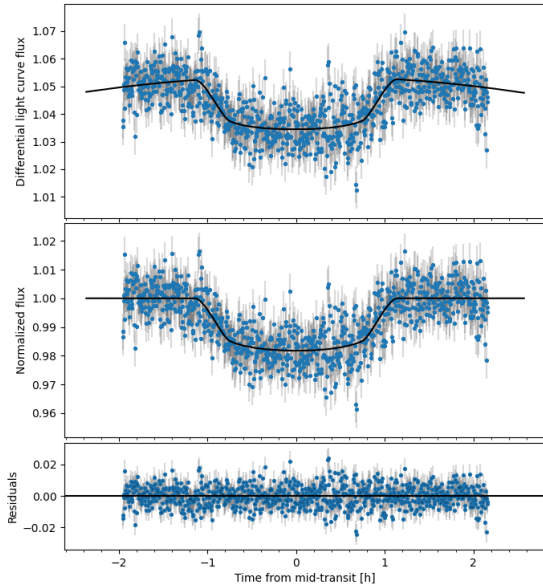


Figure 23: TASTE lightcurve

6.1 Comparison

As a further check on the output values of our analysis, we apply the (OC) method in order to compare the observed (O) central transit time (from TASTE observations) to the expected calculated (C) value (TESS results).

We obtain a O-C value of -0.010331 which indicates the accuracy of our analysis.

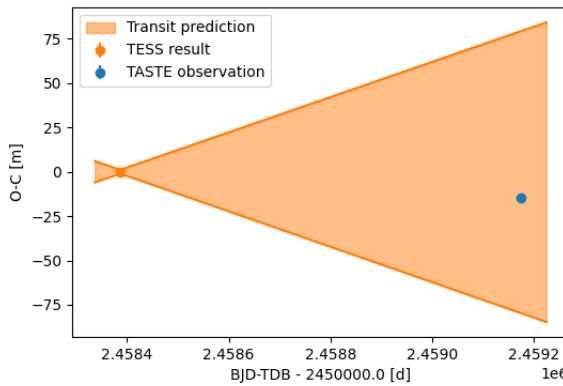


Figure 24: O-C plot: checking compatibility between TESS prediction and TASTE result.

The plot shows the propagation of the error on TESS prediction, increasing throughout time up to the epoch of our TASTE measurement. See that TASTE result falls within the cone, proving compatibility of the two results.

7 Radial velocity analysis

Knowing the RV semi-amplitude K_* and the mass M_* of the star, the planetary mass M_p is obtained by inverting the following equation.

$$K_* = \frac{1}{\sqrt{1-e^2}} \frac{M_p \sin i}{(M_* + M_p)^{2/3}} \left(\frac{P}{2\pi G} \right)^{-1/3} \quad (1)$$

where $M_p \sin i$ represents a *minimum mass* estimate. i can be measured for a transiting planet, thus yielding M_p . Only one radial velocity time series is available at NASA Exoplanet Archive⁸, involving 17 points and based on optical band spectral measurements (Anderson et al. 2011). CORALIE spectrograph mounted on the 1.2-m Euler-Swiss telescope was used in 2010 to gather the 17 spectra that lead to this RV dataset. We made sure the time range of this set did not overlap with the time range of the transits: any stellar spectra taken while the planet is transiting is missing a contribution and can no longer be considered as a RV datapoint. We ran PyORBIT again to fit the RV curve with a proper model. Radial velocity input file can be equipped with an extra "0" column, in order to enable the code to compute any RV offset due to the peculiar velocity of the star. Two models were exploited for the analysis: *radial velocities* and *harmonics*. They yield very similar results

Par	Value	σ_-	σ_+
σ_{jit}	8.2	-5.7	8.8
$v_{off}(m/s)$	-4044.0	-6.6	7.1
$P(d_{BJD})$	2.42381	-0.00002	0.00002
$T_c(d_{BJD})$	2458386.5782	-0.0007	0.0007
$K(m/s)$	137.4	-10.4	10.2

Table 3: Physical parameters obtained for *radial velocities* model.

both in terms of value and error (full results in

⁸<https://exoplanetarchive.ipac.caltech.edu/>

Par	Value	σ_-	$\sigma_+ \mathbf{8}$	Conclusions
σ_{jit}	8.4	-5.7	9.0	
$v_{off}(m/s)$	-4043.7	-7.0	7.2	Best estimates for P and Tc, check with literature
$P(d_{BJD})$	2.42381	-0.00002	0.00002	more conclude something about LD coefficients
$T_c(d_{BJD})$	2458386.578202	-0.0007	0.0007	
$K(m/s)$	137.1	-14.1	13.0	
Stellar par	Value	σ_-	σ_+	
$P(d_{BJD})$	2.4239	-0.0002	0.00002	Morton, T.D. (2015). eprint: 1503.010
$phase$	7.0	-2.2	2.1	Claret, A. et al. (2011). <i>A&A</i> 529 , A75
				Claret, A. (2017). <i>A&A</i> 600 , A30
				Claret, A. (2018). <i>A&A</i> 618 , A20
				Anderson, D.R. et al. (2011). <i>MNRAS</i> 422
				Sousa, S.G. et al. (2011). <i>A&A</i> 533 , A141
				Jenkins, J.M. et al. (2016). <i>Software and Cyberinfrastructure for Astronomy IV</i> 9913
				Hippke, M. et al. (2019a). <i>Astrophysics Journal</i> 158 , p. 143
				Hippke, M. et al. (2019b). <i>A&A</i> 623 , A39
				Malavolta, L. et al. (2016). <i>A&A</i> 588 , A118
				Malavolta, L. et al. (2018). <i>The Astronomical Journal</i> 155 , p. 107
				Kreidberg, L. (2015). <i>PASP</i> 127 , p. 1161
				Foreman-Mackey (2013). <i>PASP</i> 125 , pp. 306–312

Table 4: Physical parameters obtained for *harmonics* model.

C.1), but the simplest model yields results with slightly smaller errorbars. These are a period $P = 2.42381 \pm 0.00002d$ and a central transit time $T_c = 2458386.5782 \pm 0.0007d$.

References

A Limb darkening analysis

A.1 Claret 2017

We can represent data tables in Claret 2017 as 2D histograms, after proper unfolding of the data tables attached to the paper. To do that, we first fix metallicity, then gravity and see how the corresponding LD coefficients c_1 and c_2 depend on all three atmospheric parameters.

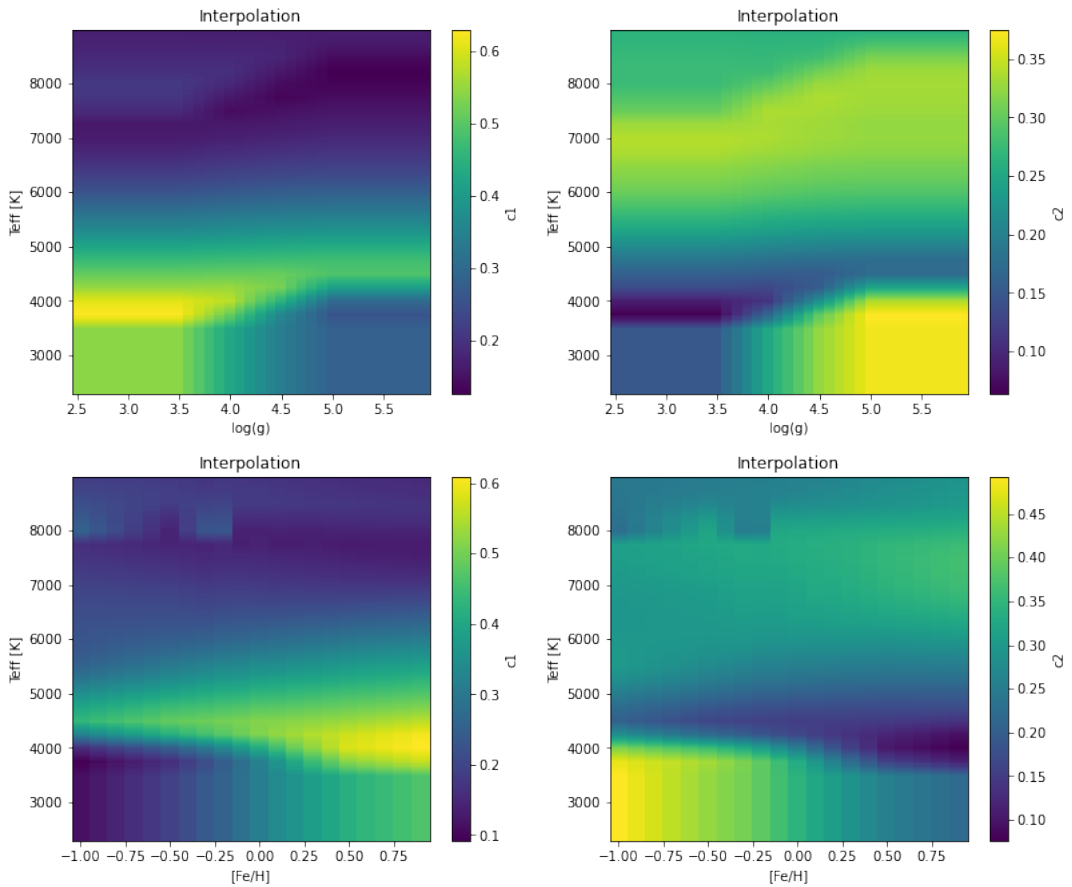


Figure 25: LD coefficient with fixed metallicity (top panels), fixed gravity (bottom panels)

We immediately visualize a vertical gradient rather than a horizontal one, showing that temperature dependence is very strong. Turns out LD coefficients are essentially a function of temperature, and minor dependences on gravity and metallicity can be barely appreciated.

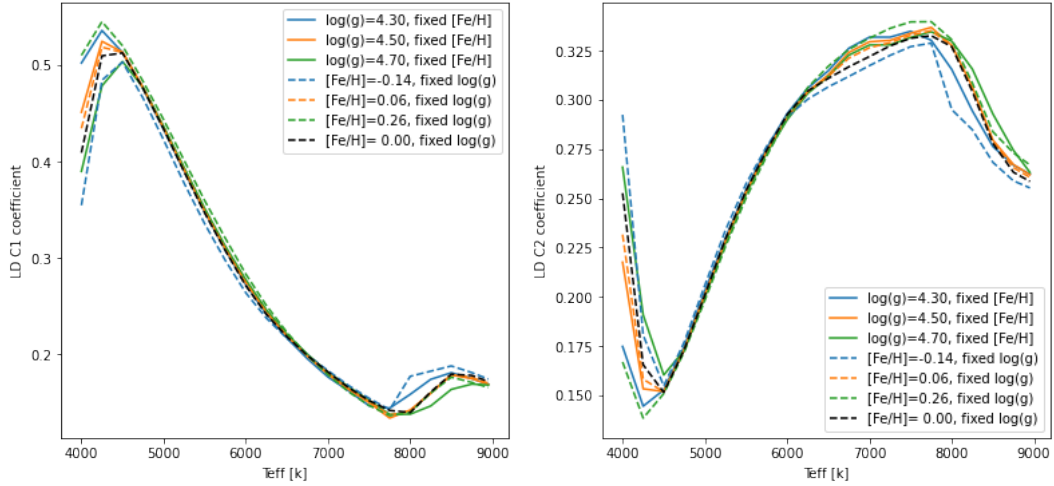


Figure 26: LD coefficient as a function of atmospheric parameters. Curves deviate at $T \leq 4500K$ and $T \geq 8000K$. Central part of the function is not sensitive to gravity and metallicity, both for c_1 and c_2 .

A relevant dependance on gravity and metallicity can only be noticed at high temperatures, where we should carefully select the proper curve. However, in the range we're interested in ($\approx 5400K$) the curve is degenerate and the choice of these parameters is secondary.

We perform a Montecarlo simulation, generating 1000 random atmospheric parameters around the actual ones, using the reference errorbar, thus conserving the error scale. This expedient will enable us to consider the result of this analysis as a good physical estimate of the LD coefficients. Even in this case we see that the distribution of the fixed-metallicity estimates is almost overlapping with the fixed-gravity one, thus confirming that, according to the exploited table, c_1 and c_2 not very sensitive on metallicity and gravity.

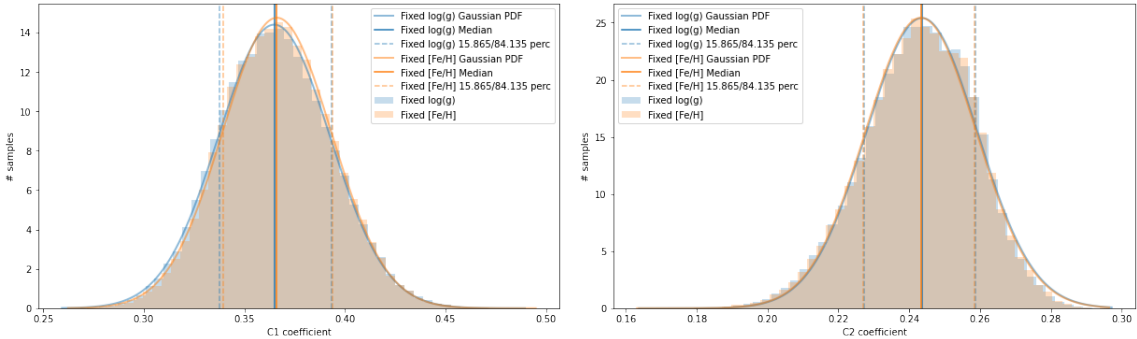


Figure 27: Montecarlo simulation for c_1 (left) and c_2 (right), for fixed metallicity and for fixed gravity.

	c_1	σ_{c_1}	c_2	σ_{c_2}
Fixed $[Fe/H]$ Median	0.3662	0.0271	0.2433	0.0157
Fixed $\log g$ Median:	0.3648	0.0277	0.2436	0.0157

For both coefficients, the two estimates coming from metallicity and gravity fixing are well compatible, thus authorizing a weighted average: $c_1 = 0.366 \pm 0.019$ and $c_2 = 0.243 \pm 0.011$.

Another way to deal with the same table is by selecting from the set two values of metallicity or gravity, an upper and lower limit, instead of just one reference value. This way we build two matrices and interpolate between the two to get to the desired result. The rest of the procedure is identical, leading to similar estimates of the LD coefficients.

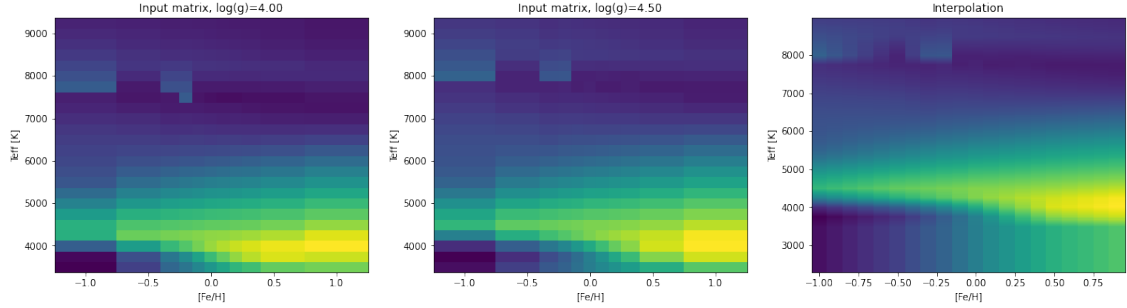


Figure 28: Matrices obtained by fixing gravity to $\log g = 4.0$, and to 4.5 , plus the interpolated matrix

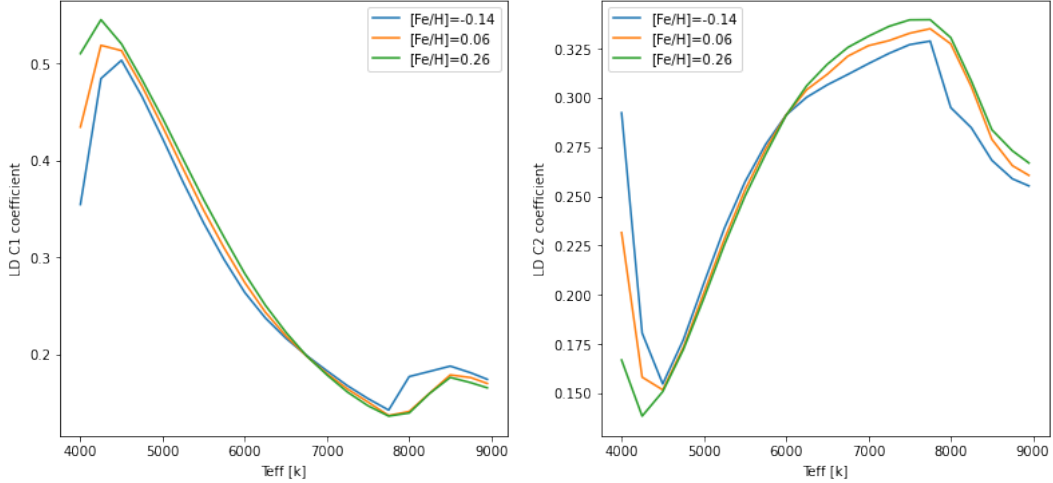


Figure 29: LD coefficients trend in the $T_{eff} - [Fe/H]$ plane

Degeneracy is less pronounced if we treat data this way. In fact, changing secondary atmospheric parameters (g and $[Fe/H]$) now produces a still modest, but visible scatter. This is confirmed by the Montecarlo analysis, that yields results compatible with the previous case but with larger errorbars.

	c_1	σ_{c1}	c_2	σ_{c2}
Fixed $\log g$ Median:	0.3650	0.0276	0.2436	0.0156

The procedure could be repeated in the same way by fixing metallicity instead.

A.2 Claret 2018

A followup paper (Claret 2018) provided a new method to model the LD coefficients dependency on atmospheric parameters. We'd like to check if this leads to different results with respect to Claret 2017. Unfolding the table requires the same procedure we've already described. Just note that in both cases we fix metallicity, and for the 2018 table metallicity must be fixed to 0, since the method is conceived for zero-metallicity stars.

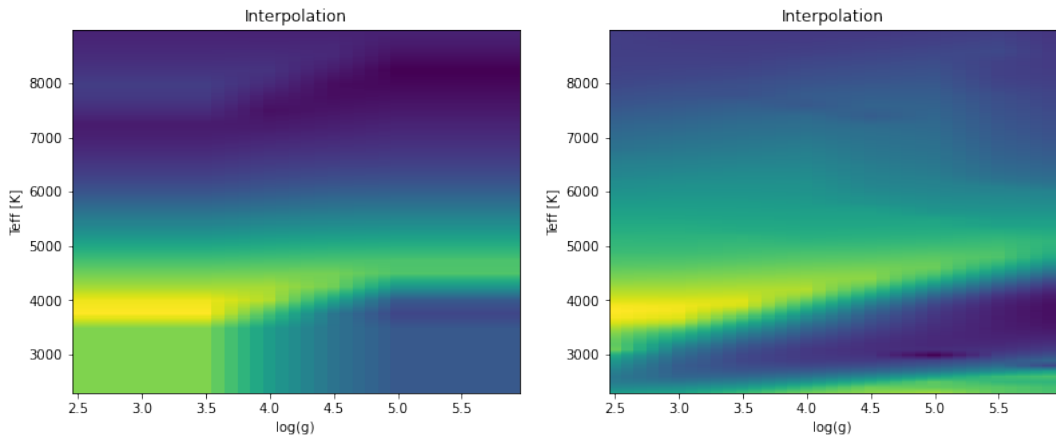


Figure 30: Comparison between interpolated matrices at fixed metallicity, to the stellar metallicity (2017 left), and to 0 (2018 right).

And finally we can display the dependency of the LD coefficients for the two-parameters game.

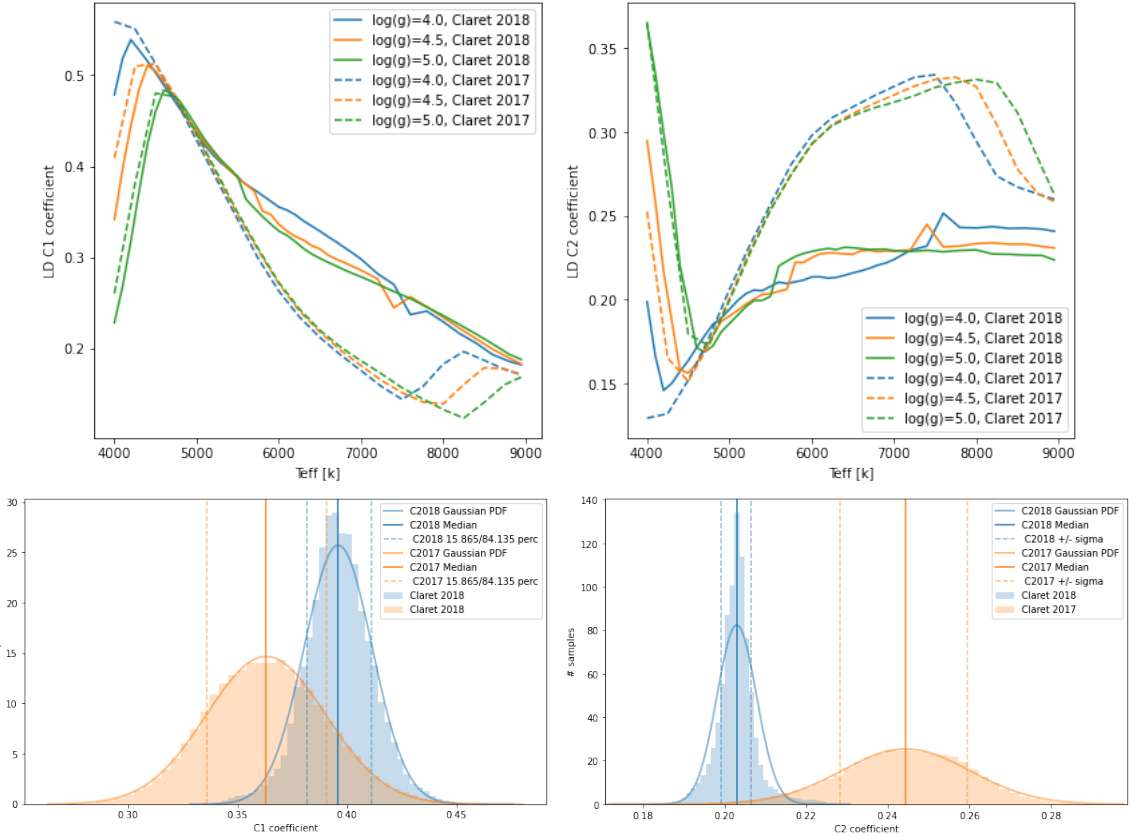


Figure 31: c_1 and c_2 trend, and comparison between the final results. Gaussian bells of the 2018 model are narrower.

First, the degeneracy on g and $[Fe/H]$ is completely removed, so that they can no longer be referred to as "secondary parameters". The comparison above shows that choosing the model will influence, even strongly, the estimate of the parameters. Quantitatively, the region characterised by $T \approx 5400K$ is one of the least affected by model choice, but the difference is still too wide to be neglected. The final estimates for the parameters are also quite different, both in terms of value and in terms of error. This indicates a systematic difference caused by the choice of the model. Because of this, we need to artificially inflate the error before using limb darkening parameters. This is very important especially for shallow transits like ours. Anyway, they're largely compatible still: see how each value is within a few errorbars away from the other. The model from Claret 2018 yields results with smaller errorbars for both coefficients.

	c_1	σ_{c1}	c_2	σ_{c2}
2017 Median	0.3631	0.0272	0.2444	0.0157
2018 Median	0.3961	0.0155	0.2030	0.0048

A.3 Claret 2011

We use another table from an older paper (Claret et al. 2011) by the same author, this time including filters. The header of our dataset shows that the filter r^* was used (SDSS). Remember that transits look differently when observed through different filters, and also that boxier transits make ingress/egress time determination easier. The unfolding technique of the data pack is always the same. This time, we account for stellar models (ATLAS/PHOENIX) and interpolation technique (least squares/flux conservation), for a grand total of 4 combinations. These are the very final results.

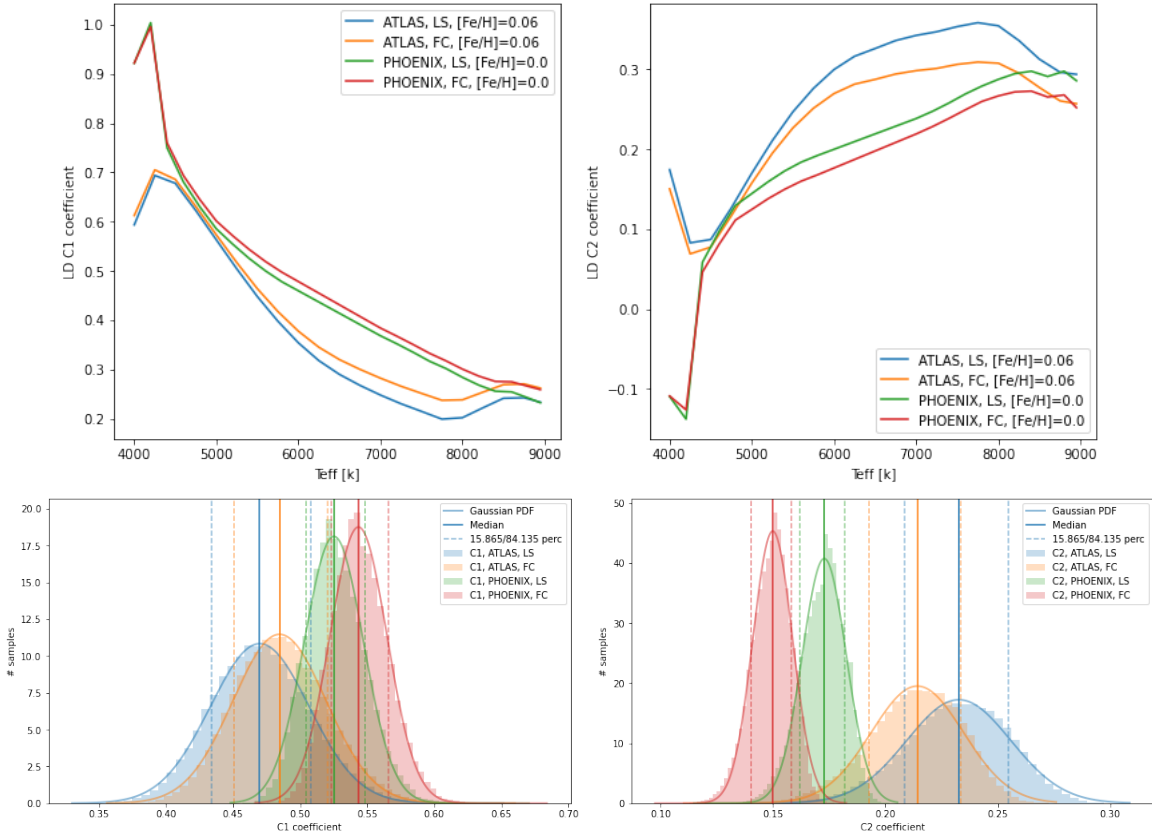


Figure 32: c_1 and c_2 trend, and comparison between the final results

Again, see how the choice of the model is deeply influencing the trend of the coefficients with respect to the atmospheric parameters, and the results consequently. Despite being compatible

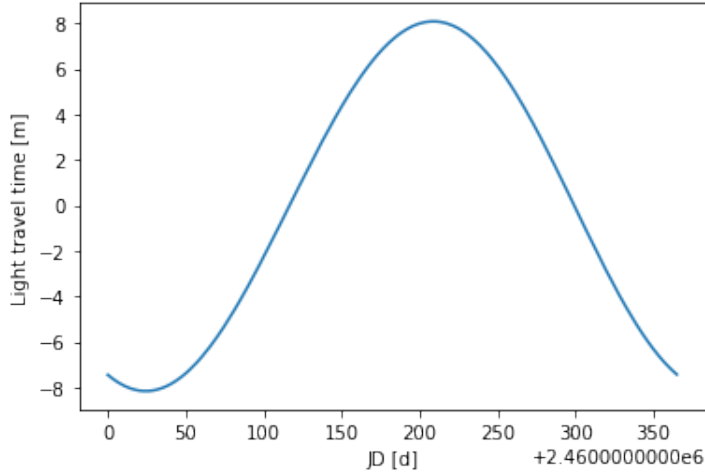
	c_1	σ_{c1}	c_2	σ_{c2}
ATLAS, LS:	0.4701	0.0367	0.2327	0.0231
ATLAS, FC:	0.4848	0.0347	0.2142	0.0205
PHOENIX, LS:	0.5251	0.0219	0.1728	0.0098
PHOENIX, FC:	0.5434	0.0212	0.1499	0.0088

between each other, the estimates of the coefficients are quite detached from the one inferred following Claret 2017 and Claret 2018. This reinforces the need to add a systematic error term. Phoenix stellar model is associated with quite thin errorbars.

B Time correction

When dealing with *sentinel.dat* output, we need to properly convert the time series, contained in columns two of the datatable. To do that, first we convert from minutes to days, then add the zero-point in Julian Date format, and finally also add half exposure time (after proper conversion in days).

Moreover, we can make use of the *Time* method to keep count of the time taken by the light to travel from the source position to the location of the observatory (Cima Ekar, Asiago). Since the Earth is in motion, light time travel is variable and follows a sinusoidal behaviour.



C Tables and figures

C.1 Radial velocity

Par	Value	σ_-	σ_+
σ_{jit}	8.186931	5.674228	8.840726
$v_{off}(m/s)$	-4044.009310	6.587574	7.142502
$P(d_{BJD})$	2.423806	0.000022	0.000021
$T_c(d_{BJD})$	2458386.578204	0.000728	0.000726
$K(m/s)$	137.437324	10.397997	10.170602

Table 5: Physical parameters obtained for *radial velocities* model.

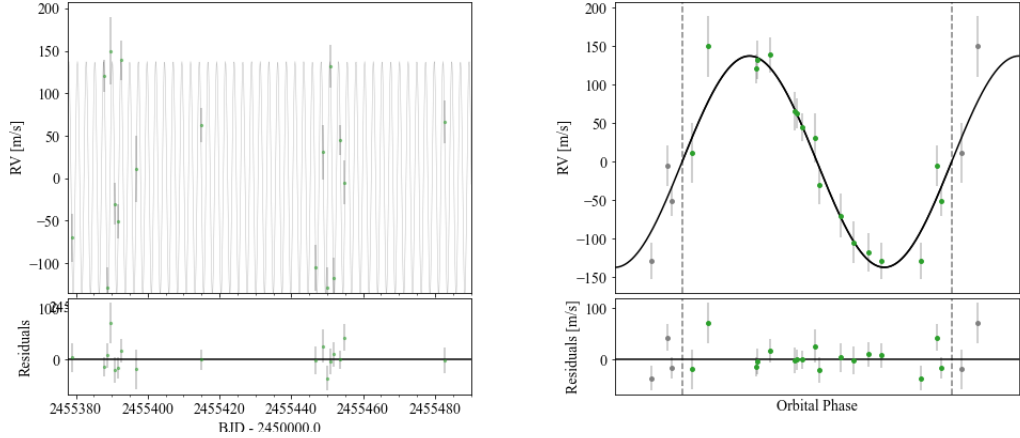


Figure 33: Radial velocities fitting, unfolded and folded *radial velocities* model.

Par	Value	σ_-	σ_+
σ_{jit}	8.412502	5.733187	9.012852
$v_{off}(m/s)$	-4043.655266	7.025075	7.166508
$P(d_{BJD})$	2.423806	0.000029	0.000028
$T_c(d_{BJD})$	2458386.578202	0.000708	0.000741
$K(m/s)$	137.052049	14.095483	13.019732
Stellar par	Value	σ_-	σ_+
$P(d_{BJD})$	2.423850	0.000166	0.000167
$phase$	7.003042	2.175383	2.084340

Table 6: Physical parameters obtained for *harmonics* model.

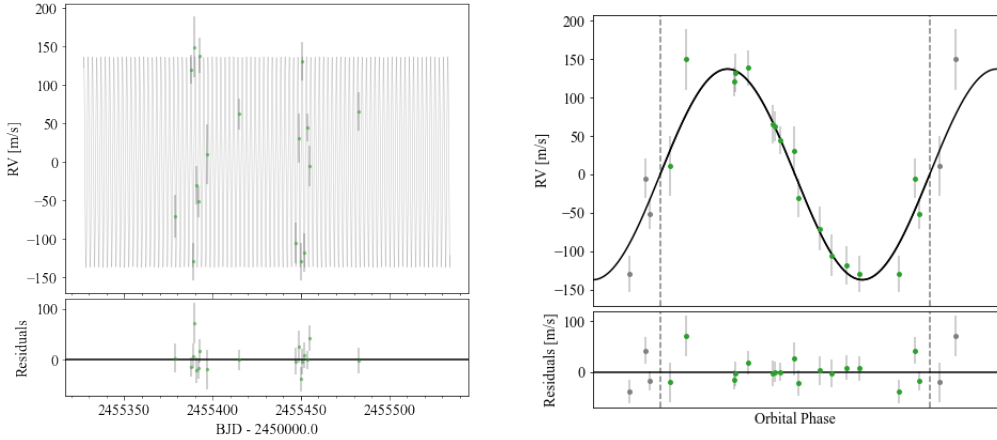


Figure 34: Radial velocities fitting, unfolded and folded *harmonics* model.

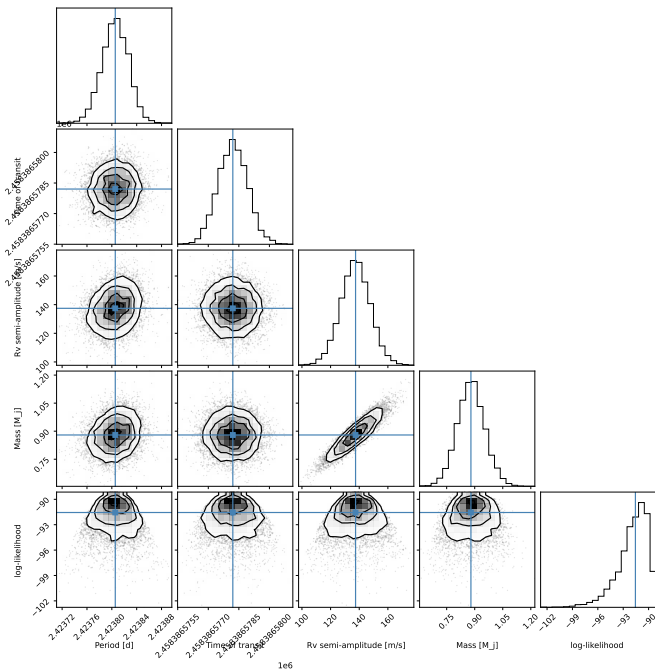


Figure 35: Correlation between parameters of the *radial velocities* model

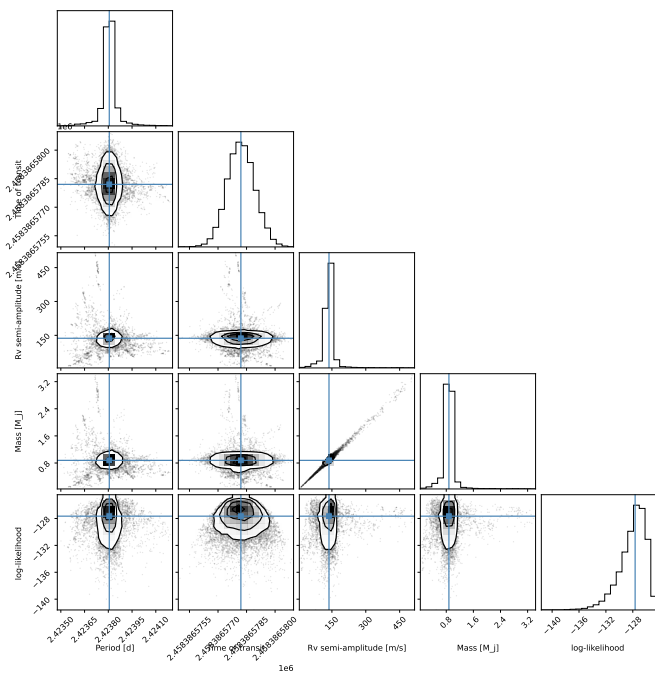
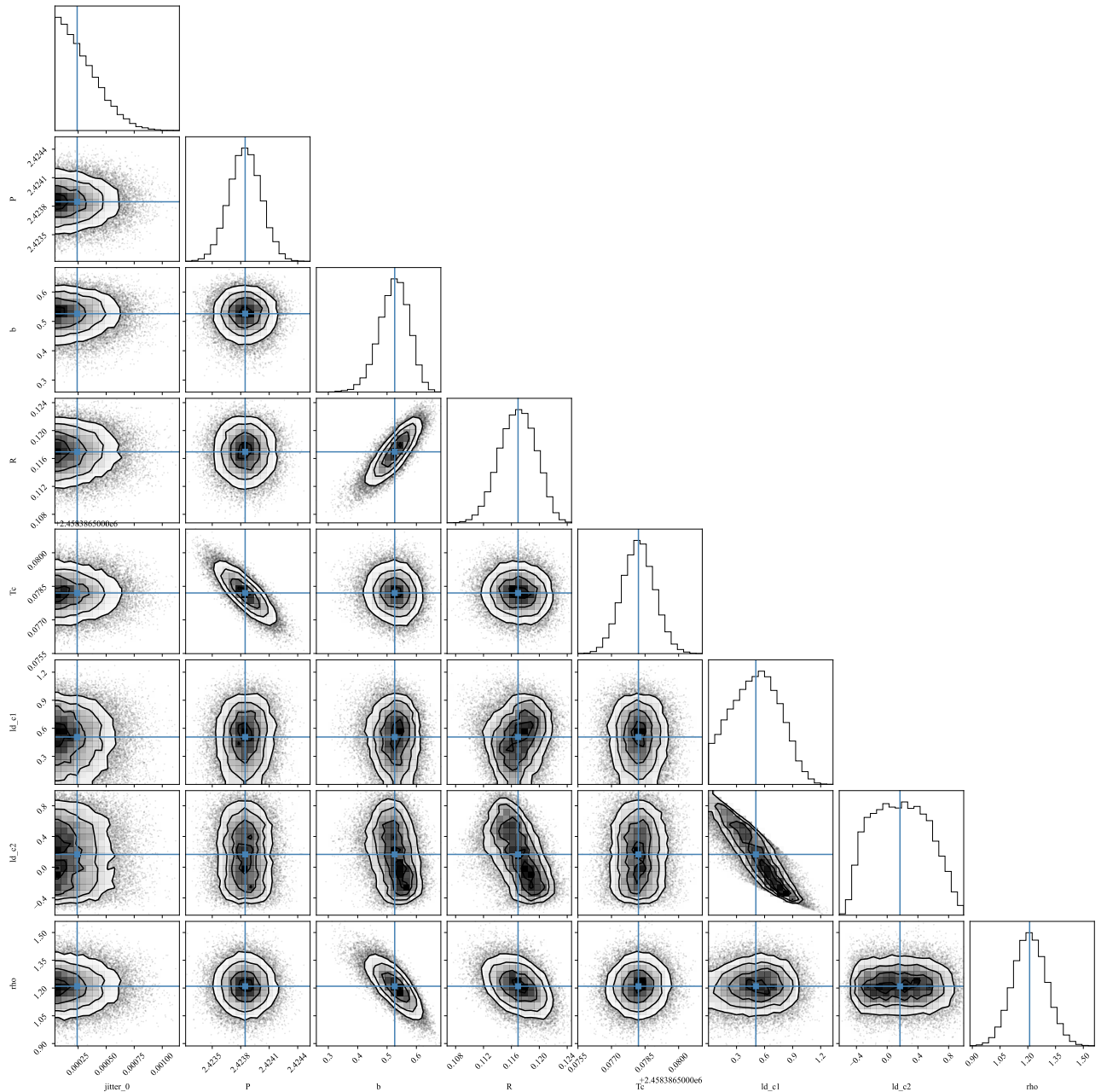


Figure 36: Correlation between parameters of the *harmonics* model

C.2 TESS and TASTE

**Figure 37:** Correlation between TESS parameters

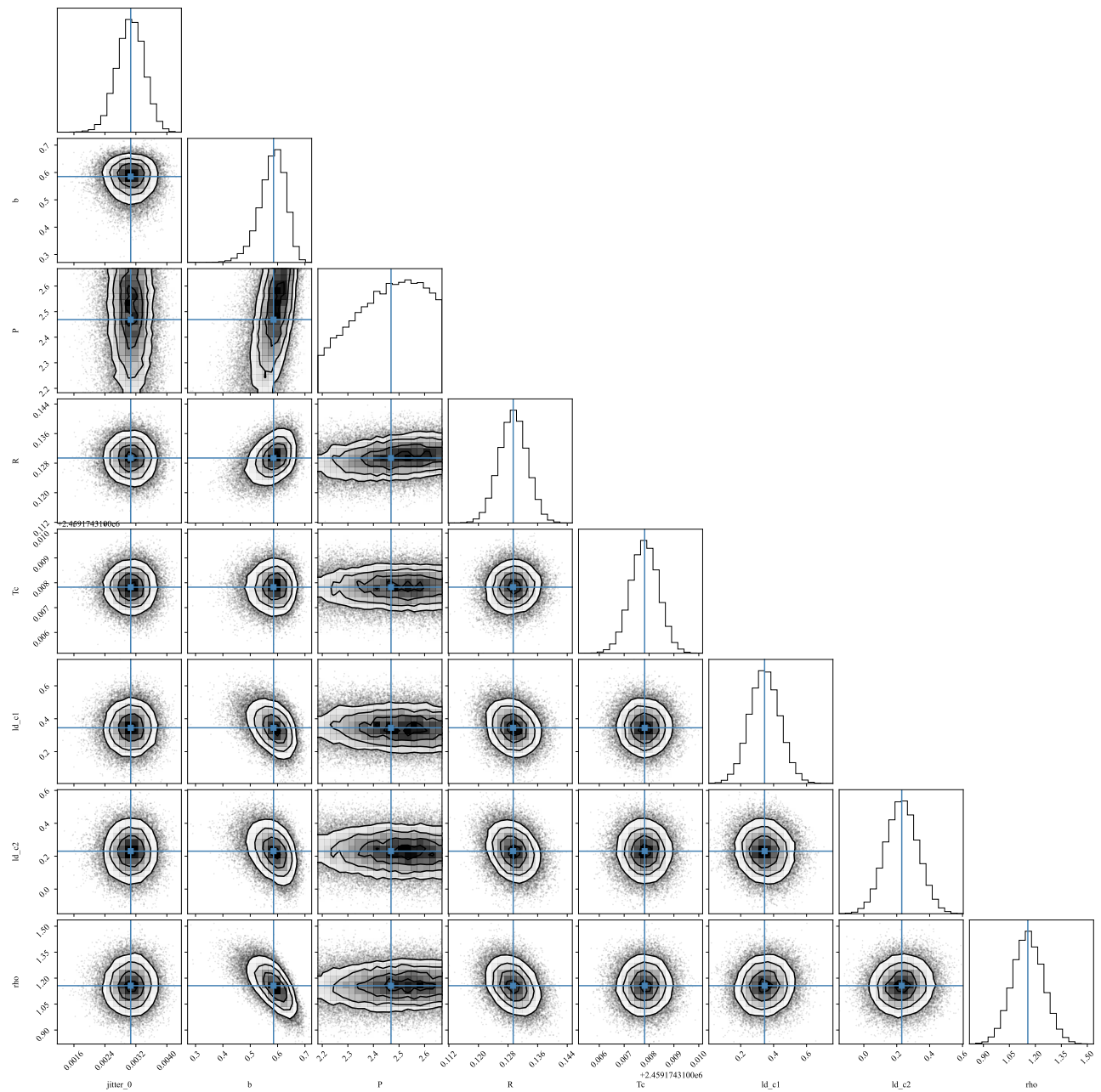


Figure 38: Correlation between TASTE parameters